DE GRUYTER Nanophotonics 2021; 10(16): 4067–4074

Research Article

Zhishen Zhang, Jiuyang Lu, Tao Liu, Jiulin Gan, Xiaobo Heng, Minbo Wu, Feng Li* and Zhongmin Yang*

Azimuthally and radially polarized orbital angular momentum modes in valley topological photonic crystal fiber

https://doi.org/10.1515/nanoph-2021-0395
Received July 22, 2021; accepted September 16, 2021;

Abstract: Artificially tailoring the polarization and phase of light offers new applications in optical communication, optical tweezers, and laser processing. Valley topological physics provides a novel paradigm for controlling electromagnetic waves and encoding information. The proposed fiber has the inner and outer claddings possessing opposite valley topological phases but the same refractive indices, which breaks through the polarization constraints of the traditional fiber. Robust valley edge states exist at the domain walls between the inner and outer claddings because of bulk edge correspondence. The valley topological fiber modes exhibit the unprecedented radial and azimuthal polarization with high-order azimuthal index. Those topological modes are robust against the disorder of the fiber structure. These results enable guide and manipulate the optical polarization and angular momentum in fiber with high fidelity. The proposed fiber has the potential to become a powerful optical spanner for the application of bio-photonics.

Keywords: azimuthally and radially polarized modes; orbital angular momentum fiber; valley topological photonic crystal.

1 Introduction

Polarization and phase are two important properties of light and spatially arranging the polarization and phase [1–3] leads to intriguing applications in optical communication [4, 5], optical tweezers [6, 7], and laser processing [8, 9]. The azimuthally and radially polarized modes [10] have the higher efficiency for the stable trapping of polar nanoparticles [6] and the laser machining in the polar materials [8]. The helically phased beams carry the orbital angular momentum (OAM) [11, 12], which have the extensive applications, such as high-capacity optical communications [5], multidimensional micro-manipulation [7], and the three-dimensional microstructure machining [9]. Recent work [1, 2, 13] has shown that the polarization and phase of light can be tailored arbitrarily in free space. Compared with the free space, the fiber has advantages in high beam quality and long transmission distance. The azimuthally/radially polarized OAM fiber will combine the advantages of the azimuthally/radially polarized lights, the OAM lights, and the fiber lights, and leads to the potential application as the low-energy great-strength optical spanner into biological tissues. However, the arbitrary combination of polarization and phase in fiber is still challenging. The polarization and phase of fiber modes rely heavily on the azimuthal index. According to the wave equation [14], the refractive indices contrast between fiber core and cladding divides the fiber modes into three categories, the linear or circular polarized modes, the azimuthally polarized modes, and the radially polarized modes. The latter two cases can only be achieved with zero azimuthal index [14]. Due to the high-order azimuthal

---

***Corresponding authors**: **Zhongmin Yang**, School of Physics and Optoelectronic Technology, South China University of Technology, Guangzhou, Guangdong 510640, China; State Key Laboratory Luminescent Materials and Devices and Institute of Optical Communication Materials, South China University of Technology, Guangzhou 510640, China; and South China Normal University, Guangzhou 510006, China, E-mail: yangzm@scut.edu.cn; and **Feng Li**, Centre for Quantum Physics, Key Laboratory of Advanced Optoelectronic Quantum Architecture and Measurement (MOE), School of Physics, Beijing Institute of Technology, Beijing 100081, China,
E-mail: phlifeng@bit.edu.cn
Zhishen Zhang, **Jiuyang Lu**, **Tao Liu**, **Jiulin Gan**, **Xiaobo Heng and Minbo Wu**, School of Physics and Optoelectronic Technology, South China University of Technology, Guangzhou, Guangdong 510640, China; and State Key Laboratory Luminescent Materials and Devices and Institute of Optical Communication Materials, South China University of Technology, Guangzhou 510640, China. https://orcid.org/0000-0002-6529-1043 (Z. Zhang)

index of the OAM modes [12], there is no report about the azimuthally and radially polarized OAM modes in fiber.

Most recently, the concept of the band structure topology [15–22] plays a new approach for controlling characteristics of the fiber modes and offers tremendous opportunities in realizing the revolutionary photonic crystal fibers (PCFs) [23–27] with low loss, novel mode field and polarization distributions, and large bandwidth. The Dirac fiber [23] modifies the envelope amplitude of fiber mode by the Dirac equation. The one-way fiber [24] perfectly immunes the backscattering loss based on the Weyl crystals. The Dirac-vortex fiber [27] supports the single polarization mode over one octave bandwidth by the vortex winding number. The valley topological photonic crystal [20, 28–35] provides an extra degree of freedom to encode the information and has been investigated in the directional optical waveguide [30–33] and the robust photonic delay line [20]. Furthermore, the paired valley topological photonic crystals for guiding the valley topological states have the same effective refractive indices, which is fundamentally different from the waveguides based on the total internal reflection [14] or photonic bandgap [36]. The valley topology may enable us to design waveguide without refractive indices contrast and obtain novel optical fibers with controllable polarization and phase.

Here, we achieve the unprecedented azimuthally and radially polarized orbital angular momentum (OAM) modes in valley topological photonic crystal fiber (TPCF). The proposed TPCF has the inner and outer claddings with the same refractive indices but opposite valley Chern numbers. By eliminating the refractive indices contrast between fiber core and cladding, the three characteristic equations for the different polarized fiber modes now have the identical expressions, which breaks through the polarization constraints of the azimuthal index in the traditional fiber. The topological fiber modes are composed of the clockwise and counterclockwise resonance of topologically protected states in the enclosed interface. The polarization of topological fiber mode is consistent with the corresponding topological state that is parallel or perpendicular to the interface. The topological fiber modes, characterized with the azimuthal/radial polarization, have high azimuthal index and synthesize the polarized OAM modes. Due to the topological protection, the polarization characteristics and the confinement losses of the fiber modes are robust to the local perturbation. These findings may enable the creation of novel polarized orbital angular momentum fiber for optical trapping and laser micromachining.

2 Results

2.1 Topological properties in quasi two dimensional (2D) systems

As depicted in Figure 1a, the design consists of a triangular lattice of the three-hole units in the transverse plane and invariant structure in the longitudinal direction. The lattice constant, the hole radius, and the center-to-center distance of the three-hole unit are set as $a = 3.1\ \mu\text{m}$, $r = 0.2a$, and $h = {}^{\sqrt{3}a}/_{6}$, respectively. The rotation angle of the three-hole α controls the topological properties of the photonic crystal. The refractive index of the substrate and holes are set as 1.444 and 1. Compared with the in-plane propagation in the 2D photonic topological insulators, the light can propagate in directions that lie outside the transverse

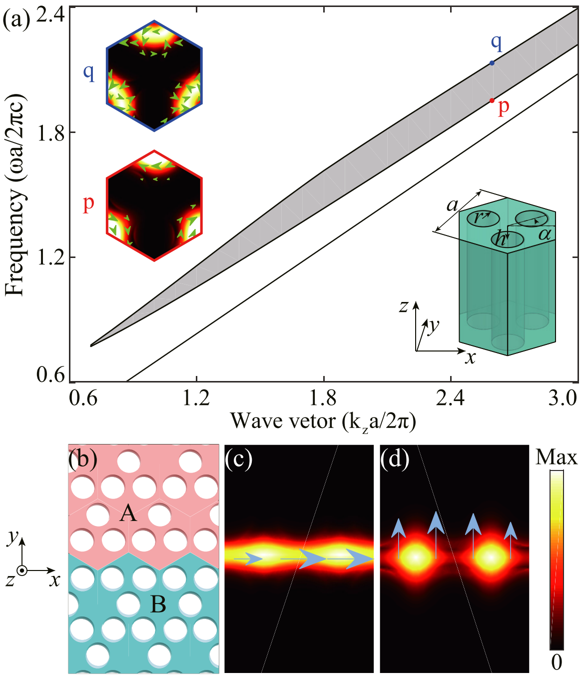

Figure 1: Topological gap and edge states with a non-zero k_z. (a) Topological bandgap (gray region) as k_z varies. The black line indicates the dispersion of the substrate material. The downright inset shows the three-hole unit. The top left insets are the electric field distributions of lower and upper bands at K point correspond to labels p and q, respectively. The green cones denote the Poynting vectors. (b) Interface formed by the upper phase A and lower phase B. (c) Electric field distribution of the horizontally polarized edge state. (d) Electric field distribution of the vertically polarized edge state. The blue arrows indicate the polarization characteristics.

section in quasi-2D systems due to the additional vertical dimension. More specifically, both the topological photonic band gap (TPBG) and edge states can be constructed under a non-zero longitudinal wave constant k_z, just like the ordinary (nontopological) photonic bandgaps and the Dirac cones [14]. The band topology of quasi-2D valley topological photonic crystal is analytically described by the effective Hamiltonian $\mathcal{H}_{K/K'} = \pm v_D(\sigma_x \delta k_x + \sigma_y \delta k_y) \pm (\Delta_1 \delta k_y + \Delta_2)\sigma_z$ (see Supplementary Information 1),where K/K' are the corner points in the first Brillouin Zone, v_{D} is the group velocity, $(\delta k_x, \delta k_y) = (k_x - K_x^{(\prime)}, k_y - K_y^{(\prime)})$ is the reciprocal vector measured from the K/K' points, $\sigma\,(x, y, z)$ are the Pauli matrices. $\Delta_1 \delta k_y$ is considered as the k_z-induced perturbation, which does not break the degenerate states at K/K' points but change the bands near the K points. Δ_2 is the structure-induced perturbation strength because of the breakdown of inversion symmetry, will lift the degenerate states at K/K' points and open a topological nontrivial gap. The k_z acts on the electromagnetic fields of the pseudospin states (insets in Figure 1a), the gap size and center frequency of topological gap, which will expand the parameter scope of the photonic topological insulators, such as reducing the requirement of the substrate refractive index. Figure 1a shows the dependence of the topological bandgap as k_z varies. The topological gap is opened with ${}^{k_z a}/_{2\pi} > 0.6$, and gradually increases to the maximum with ${}^{k_z a}/_{2\pi} = 2$.

The out-of-plane topological edge states are supported at the interface between two photonic crystals with the opposite valley Chern number. In quasi-2D valley topological photonic crystal, the band inversion occurs when the rotation angle (α) changes its plus-minus. So the photonic crystal with $-60° < \alpha < 0°$ (phase A) and $0° < \alpha < 60°$ (phase B) have the opposite valley Chern number. Figure 1b schematically shows the interface that is formed by the upper phase A and lower phase B. Two edge states (Figure 1c and d) with the horizontal and vertical polarization are achieved with ${}^{k_z a}/_{2\pi} = 2.6372$. Due to bulk-boundary correspondence, there should be only one edge state with hybrid polarization at the interface. However, the horizontally and vertically polarized component will have different longitudinal wave constant because of the shape birefringence of the interface. So this hybrid polarized edge state is further split into two horizontally and vertically polarized states. The electric fields of the edge states [37] with the out-plane propagation are expressed as

$$\boldsymbol{\varphi_x} = (c_1\psi_{1x} + c_2\psi_{2x}) \cdot \mathrm{e}^{\mathrm{i}(\delta k_x \cdot x + \delta k_y \cdot y)} \cdot \mathrm{e}^{-|m v_D y|} \cdot \mathrm{e}^{\mathrm{i}(K_{Dx}\cdot x + K_{Dy}\cdot y + k_z \cdot z)} \cdot \mathrm{e}^{-\mathrm{i}\omega_x t} \cdot \boldsymbol{e_x} \tag{1}$$

$$\boldsymbol{\varphi_y} = (c_1\psi_{1y} + c_2\psi_{2y}) \cdot \mathrm{e}^{\mathrm{i}(\delta k_x \cdot x + \delta k_y \cdot y)} \cdot \mathrm{e}^{-|m v_D y|} \cdot \mathrm{e}^{\mathrm{i}(K_{Dx}\cdot x + K_{Dy}\cdot y + k_z \cdot z)} \cdot \mathrm{e}^{-\mathrm{i}\omega_y t} \cdot \boldsymbol{e_y} \tag{2}$$

where $\psi_{1,2}$ is the electric field of counterclockwise or clockwise pseudospin states at the K points, subscript x/y represents the electric field component parallel or perpendicular to the interface, $\boldsymbol{e_{(x/y)}}$ is the unit vector, $m = {}^{\omega_{\mathrm{D}}\Delta}/_{v_{\mathrm{D}}^2}$ is the equivalent mass, and ω_{D} is the Dirac frequency. $\omega_{(x/y)}$ is the frequency of edge state, which is influenced by the wave vector (k_x, k_y, k_z) and the polarization. $(k_{\mathrm{D}x}, k_{\mathrm{D}y}, k_z)$ is the wave vector at K/K' points.

2.2 Topological fiber modes formed by the out-of-plane edge states

When the interface is rolled into the tubular structure, the forward (backward) edge state will form a stable clockwise (counterclockwise) propagation fiber mode. Mathematically, the interface contour of the TPCF is converted into the equal-perimeter circle with the coordinate transformation $(l_x, l_y) \Leftrightarrow (\theta, r - l_y)$, where $l_x = {}^{L\theta}/_{2\pi}$ is the length of interface related to the arc angle θ, L is the perimeter of the enclosed interface, and l_y is the least length to the interface. In succession, the wave vector (k_x, k_y) is also converted into $(\frac{2\pi k_\theta}{L}, k_r)$. The key of this transformation is that the global formation mechanisms of topological fiber modes are changeless although the local mode field distribution may have some deviation. So the mode is described by a cylindrical wave function [14].

$$\left(\frac{\mathrm{d}}{\mathrm{d}r^2} + \frac{1}{r^2}\frac{\mathrm{d}}{\mathrm{d}\theta^2} + \frac{1}{r}\frac{\mathrm{d}}{\mathrm{d}r}\right)\Phi + (k_\theta^2 + k_r^2)\,\Phi = 0 \tag{3}$$

It is important that the core is zero-thickness and the inner and outer claddings have the same (k_θ, k_r). So the mode field distribution Θ is proportional to $R(r)\mathrm{e}^{iv\theta}$, where

$$R(r) = \begin{cases} I_v\left(\sqrt{k_\theta^2 + k_r^2}\cdot r\right), & 0 \le r \le r_0 \\ K_v\left(\sqrt{k_\theta^2 + k_r^2}\cdot r\right), & r \ge r_0 \end{cases} \tag{4}$$

I_v and K_v are the v-th modified Bessel functions of the first and second kinds, and $r_0 = {}^{L}/_{2\pi}$. Due to the same subexpressions inside the I_v and K_v, the characteristic matrix of the equations formed by the boundary condition of continuity is singular and the polarization of fiber mode is not determined (see Supplementary Information 2). The polarization properties of fiber modes are directly derived from the out-of-plane edge states in the enclosed interface between the inner and outer claddings. The horizontally and vertically polarized edge states are converted into the radially and azimuthally polarized modes in TPCF. The longitudinal electric field in TPCF is

$$E_z(\theta,r) \propto u_e(\theta,r)\cdot \mathrm{e}^{\mathrm{i}\theta_e(\theta,r)}\cdot \mathrm{e}^{-|mv_D(r-r_0)|}\cdot \mathrm{e}^{\mathrm{i}(k_\theta\cdot\theta)}\cdot \mathrm{e}^{\mathrm{i}[k_r(r-r_0)]}\cdot R(r) \tag{5}$$

where $u_e(\theta,r)\cdot \mathrm{e}^{\mathrm{i}\theta_e(\theta,r)}$ is the initial distribution of the edge state. When the θ ranges from 0 to 2π, the additional phase difference induced by the edge state is 0. So the k_θ should be the integer v for keeping the periodicity in the azimuthal direction, which coincide with the phase distribution of the OAM modes in TPCF (Figure 3). In other words, only the edge states that meet the resonance condition can form the fiber modes. The vector modes in TPCF are the interference patterns resulting from the clockwise and counterclockwise rotation of topologically protected states in the enclosed interface between the inner and outer claddings.

2.3 Radially and azimuthally polarized OAM modes in TPCF

Figure 2a shows the cross-section of valley topological photonic crystal fiber, whose inner and outer claddings are the phase A and phase B, respectively. The fiber core interface is set as the triangle-clique instead of the hexagon to avoiding that two kinds of interfaces appeared alternately. The layers of the inner and outer claddings are respectively set as 2 and 5, and the parameters of units are the same as Figure 1a. The optimization of the fiber structural parameters is shown in Supplementary Information 3. The fiber vector modes at 1550 nm are computed by the finite element method. As shown in Figure 2, the proposed TPCF supports multiple fiber modes in topological gap. The topological fiber modes are classified as the azimuthally polarized ($\mathrm{AP}_{vm}^{e/o}$) and radially polarized ($\mathrm{RP}_{vm}^{e/o}$) modes, as the $\mathrm{HE}_{vm}^{e/o}$ and $\mathrm{EH}_{vm}^{e/o}$ modes in conventional fibers, where the subscript v and m are the azimuthal and radial indices, the superscript e and o represent the even and odd vector modes. It is important that those unique radially and azimuthally polarized modes in TPCF are resulted from the single polarization of the topologically protected edge states, but not the enclosed contour shape of fiber core. To prove that assertion, the triangle-clique core fiber is designed and multiple hybrid polarized modes are observed (Supplementary Information 4). Also, the polarized modes in TPCF can be the higher azimuthal index, which are fundamentally different from the TE_{0m} and TM_{0m} mode in conventional fibers, whose eigenvalue equations limit the zero azimuthal index. For each azimuthal index, there are two degenerate modes (the even and odd modes) with the same propagation constant due to two complementary interference patterns of the clockwise and counterclockwise edge states. However, when the number of bright spots in fiber mode is the multiples of three, this degeneracy is lifted due to the C_{3v} symmetry of the fiber cross-section. As shown in Figure 2b and c, the AP_{vm} and RP_{vm} modes have the similar electric field distributions and orthogonal polarization distributions, for both fundamental modes (AP_{11}^{o} and RP_{11}^{o}) and the high order modes (AP_{21} and RP_{21}). All the modes in the proposed fiber have the confinement loss no more than the magnitude of 5×10^{-4} dB/km. The higher azimuthal index (v) of mode is, the larger confinement loss is. The $\mathrm{AP}_{vm}^{e/o}$ modes have the less confinement loss than the $\mathrm{RP}_{vm}^{e/o}$ modes.

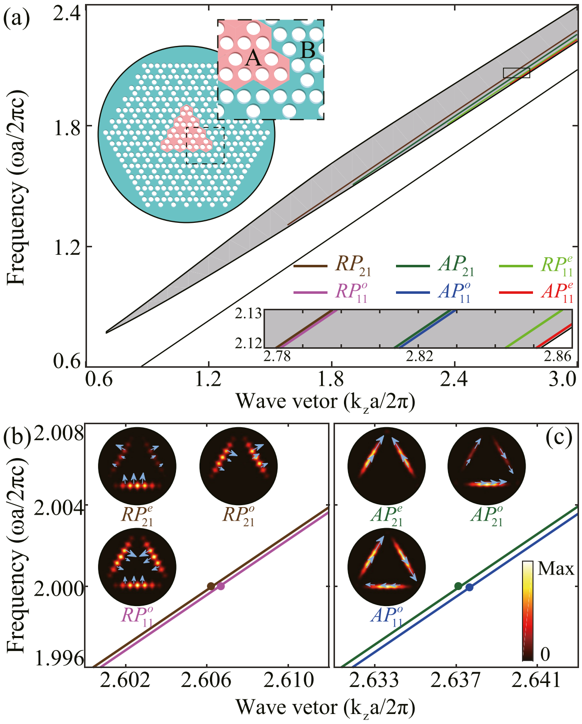

Figure 2: Azimuthally and radially polarized modes in TPCF. (a) Fiber dispersion in topological gap. The top left inset is the structure of the valley topological photonic crystal fiber. The downright inset is the enlarged view of fiber dispersion in solid line box. (b) Dispersions and the electric field distributions of the RP_{11}^{o}, RP_{21}^{e}, and RP_{21}^{o} modes. (c) Dispersions and the electric field distributions of the AP_{11}^{o}, AP_{21}^{e}, and AP_{21}^{o} modes. The blue arrows indicate the polarization characteristics.

The unprecedented radially and azimuthally polarized orbital angular momentum (OAM) fiber modes are created based on the synthetic formula [38] (even mode ± $i\cdot$ odd mode) for the degenerate modes. For example, Figure 3 shows the electric field and phase distributions of the azimuthally and radially polarized OAM modes

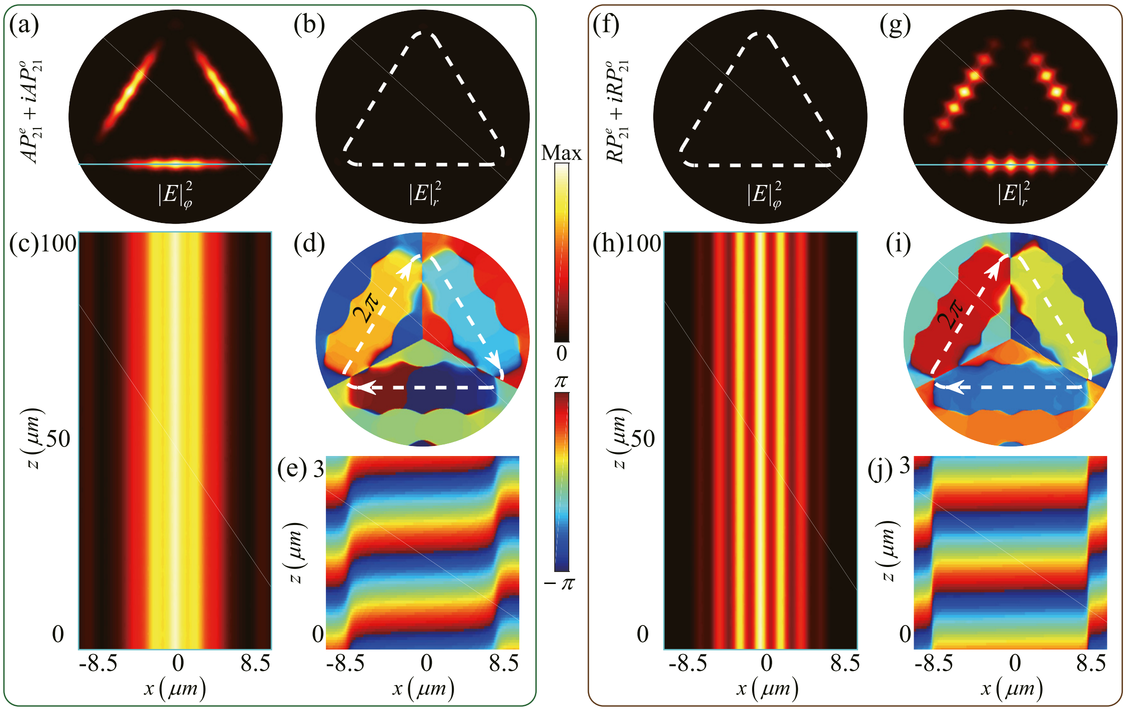

Figure 3: Azimuthally and radially polarized orbital angular momentum fiber modes. (a–e) Azimuthal electric field, radial electric field, propagating electric field, phase distribution, and propagating phase of APOAM_{11}^{+}; (f–j) Azimuthal electric field, radial electric field, propagating electric field, phase distribution, and propagating phase of RPOAM_{11}^{+}. The blue lines in (a) and (g) donate the location of the vertical sections for the propagating fields.

in TPCF with topological charge $l = 1$, which are synthesized by $\text{APOAM}_{l-1,1}^{\pm} = \text{AP}_{l1}^{e} \pm i \cdot \text{AP}_{l1}^{o}$ and $\text{RPOAM}_{l-1,1}^{\pm} = \text{RP}_{l1}^{e} \pm i \cdot \text{RP}_{l1}^{o}$. The differences among the effective indices of the adjacent modes are larger than 1×10^{-4}, which will greatly decrease the mode coupling. The spiral phase distribution (Figure 3d and i) validates that the topological charge of OAM mode is $l = 1$. As shown in Figure 3a and b, the energy mainly concentrates to the azimuthal component. The polarization extinction ratio is defined as $\text{PER} = {}^{P_1}/_{P_2}$, where P_1 and P_2 are the power of major and minor polarization components, respectively. For the APOAM_{11}^{+} mode, the polarization extinction ratio is 20 dB. For the RPOAM_{11}^{+} mode (Figure 3f and g), the energy mainly concentrates to the radial component and the polarization extinction ratio is 17.9 dB. To investigate the propagation feature of APOAM_{11}^{+} and RPOAM_{11}^{+} modes, we further simulate the transmissions of OAM modes along the proposed TPCF (100 μm long) based the finite-difference time-domain method. As shown in Figure 3c and h, both polarized OAM modes propagate stably without attenuation. The helical phase distributions (Figure 3e and j) are coincident with Figure 3d and i, which indicate that both modes have the helical wavefront and propagate in spiral manner. The azimuthally and radially polarized OAM modes are remarkably different from the linear and circular polarization OAM modes in the reported OAM fiber. Proposed valley topological photonic crystal fiber brings new development potential for the OAM fiber applications such as the optical trapping and laser micromachining.

The modes in TPCF are topologically robust against the structure disorder. In order to show this stability, we introduce the random offset $\in (-\delta, \delta)$ to TPCF in the random directions (Figure 4a inset). For each δ, 40 simulations are conducted. Figure 4 shows the polarization extinction ratio and confinement loss of AP_{21} mode in the defective TPCFs. The fluctuating ranges of both two cases slowly increase with the increasing δ. When ${}^{\delta}/_{h}$ is 3%, the polarization extinction ratio is higher than 15 dB and the confinement loss is less than 0.003 dB/km, which is enough for most OAM applications. The performance deterioration in the defective TPCFs is because of the coupling between the AP_{21} mode and the leaky modes triggered by the disordered fiber claddings. This coupling effect is greatly inhibited for two reasons. First, the defect modes are not allowed in the topological gap unless the symmetry for the topological protection is broken. Therefore, the difference between the equivalent refractive indices of the AP_{21} mode and the leaky modes increases. Second, there is the phase mismatch

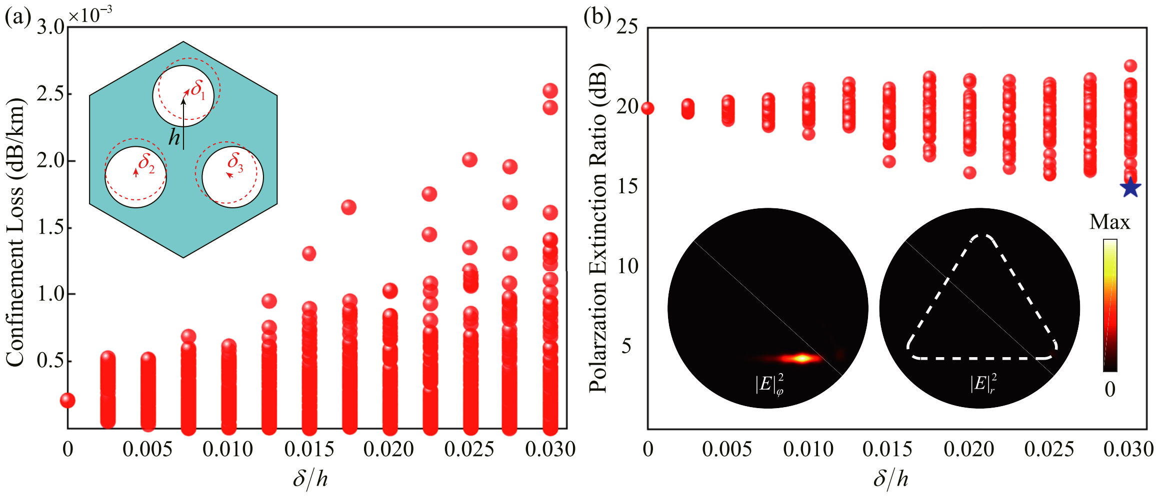

Figure 4: Fiber modes against the in-plane disorder. (a) Confinement loss of AP_{21} mode of TPCF. All holes in fiber occur the random offsets δ and inset shows the disorder cell with the red dashed lines. h is the distance between the hole and the center of cell. (b) Polarization extinction ratio of AP_{21} mode of TPCF. Insets are the azimuthal and radial electric field of the perturbed AP_{21} mode, whose polarization extinction ratio is labeled by the star.

between the AP_{21} mode and the leaky modes. Although the disorder only causes less coupling between two oppositely directed topological modes, the clockwise topological resonance modes propagating in the disordered TPCF can turn into the counterclockwise modes. The disorder will destroy the degeneration of the even mode and odd mode, and introduces the additional phase difference. Based on the synthetic formula (even mode $\pm i \cdot$ odd mode), the rotation direction of mode will be changed when the additional phase difference equal to π. It is worth emphasizing that the TPCF is not a one-way waveguide due to the invariant structure along the propagating direction. The backscattering wave can be excited with the longitudinal nonuniform defects.

3 Discussion

For experimental considerations, the proposed TPCF can be realized by the stack-and-draw method, which has been used for fabricating various PCFs with circular holes array. Due to the non-zero longitudinal wave constant, the TPBG is formed with the relatively low index contrast. So the TPBG can be constructed by numerous glasses, such as SiO_2, Schott SF_4, and As_2S_3. The operating wavelength can be turned to arbitrary transparent band of substrate materials by adjusting the size of primitive cell in claddings. While the above analysis has been limited to the valley topological photonic crystal with three-holes units, other 2D photonic topological insulators, such as the photonic crystals with C_{6v}-symmetric unit cells [18], can also be implemented for the TPCF with the same guiding mechanism.

In conclusion, a novel TPCF is proposed with the radially and azimuthally polarized orbital angular momentum (OAM) fiber modes. The proposal TPCF is composed of inner and outer claddings that are the honeycomb lattices with the upwards and downwards three-holes units. The guiding mechanism based on the topologically protected edge state is established and the topological fiber modes are studied systematically. Due to the topological protection, the modes of the TPCF are robust against the in-plane disorder. The proposal TPCF further enriches the principles of fiber design, by enhancing the performances through controllable modes, polarization, and defect-immune propagation feature. It also offers a new platform for exhibiting the novel topological phenomena in quasi-2D systems.

4 Methods

Our simulations were performed by the COMSOL RF module and the Lumerical FDTD Solutions. The bandgaps in Figure 1a was calculated by a hexagonal primitive cell with different k_z-vector under the Floquet periodic boundary conditions. The electric field distributions of the edge states (Figure 1c and d) were calculated by the interface formed by the upper phase A (1×10 units) and lower phase B (1×10 units) with $(k_x, k_y, k_z) = ({}^{2\pi}/_{3a}, 0, {}^{2\pi}/_{2.6372a})$. The dispersions and the electric field distributions of fiber modes (Figures 2 and 4) were calculated by the cross-section (Figure 2a inset) with the perfectly matched layer. In the defective fiber simulations, all holes in fiber occur the random offsets δ. The confinement loss was calculated by $L_{\text{loss}} = \frac{20}{\ln 10} \cdot \frac{2\pi}{1.55\times10^{-6}} \cdot \text{Im}[n_{\text{eff}}] \times 10^3(\text{dB/km})$, where $\text{Im}[n_{\text{eff}}]$ was the imaginary part of the mode equivalent refractive index. The OAM fiber modes (Figure 3a, b, and d) were synthesized by $\text{APOAM}_{11}^{+} = \text{AP}_{21}^{e} + i \cdot \text{AP}_{21}^{o}$ and the modes (Figure 3f, g, and i) were synthesized by $\text{RPOAM}_{11}^{+} = \text{AP}_{21}^{e} + i \cdot \text{AP}_{21}^{o}$. The propagating electric field and phase of OAM fiber modes (Figure 3c, e, h, and j) were calculated by a three-dimensional FDTD model (the proposed fiber with 100 μm long) and the perfectly matched layer boundary conditions were used. The mode sources were set as $\text{AP}_{21}^{e} + i \cdot \text{AP}_{21}^{o}$ and $\text{RP}_{21}^{e} + i \cdot \text{RP}_{21}^{o}$, respectively.

Author contribution: All the authors have accepted responsibility for the entire content of this submitted manuscript and approved submission.

Research funding: The authors gratefully acknowledge financial support from NSFC Development of National Major Scientific Research Instrument (61927816), Guangdong Key Research and Development Program (2018B090904001, 2018B090904003), National Natural Science Foundation of China (NSFC) (U1609219, Grants No. 12074446), Local Innovative and Research Teams Project of Guangdong Pearl River Talents Program (2017BT01X137); Project funded by China Postdoctoral Science Foundation (2019M652872), and the Fundamental Research Funds for the Central Universities (2018ZD01).

Conflict of interest statement: The authors declare no conflicts of interest regarding this article.

References

[1] A. Arbabi, Y. Horie, M.Bagheri, and A.Faraon, "Dielectric metasurfaces for complete control of phase and polarization with subwavelength spatial resolution and high transmission," *Nat. Nanotechnol.*, vol. 10, pp. 937–943, 2015.

[2] J. B. Mueller, N. A. Rubin, R. C. Devlin, B. Groever, and F. Capasso, "Metasurface polarization optics: independent phase control of arbitrary orthogonal states of polarization," *Phys. Rev. Lett.*, vol. 118, p. 113901, 2017.

[3] M. Principe, M. Consales, A. Micco, et al., "Optical fiber meta-tips," *Light Sci. Appl.*, vol. 6, p. e16226, 2017.

[4] W. Qiao, T. Lei, Z. Wu, S. Gao, Z. Li, and X. Yuan, "Approach to multiplexing fiber communication with cylindrical vector beams," *Opt. Lett.*, vol. 42, pp. 2579–2582, 2017.

[5] Z. Xie, T. Lei, F. Li, et al., "Ultra-broadband on-chip twisted light emitter for optical communications," *Light Sci. Appl.*, vol. 7, p. 18001, 2018.

[6] H. Moradi, V. Shahabadi, E. Madadi, E. Karimi, and F. Hajizadeh, "Efficient optical trapping with cylindrical vector beams," *Opt. Express*, vol. 27, pp. 7266–7276, 2019.

[7] S. Mei, K. Huang, T. Zhang, et al., "Evanescent vortex: optical subwavelength spanner," *Appl. Phys. Lett.*, vol. 109, p. 191107, 2016.

[8] E. Skoulas, A. Manousaki, C. Fotakis, and E. Stratakis, "Biomimetic surface structuring using cylindrical vector femtosecond laser beams," *Sci. Rep.*, vol. 7, pp. 1–11, 2017.

[9] J. Ni, C. Wang, C. Zhang, et al., "Three-dimensional chiral microstructures fabricated by structured optical vortices in isotropic material," *Light Sci. Appl.*, vol. 6, p. e17011, 2017.

[10] Q. Zhan, "Cylindrical vector beams: from mathematical concepts to applications," *Adv. Opt. Photon*, vol. 1, pp. 1–57, 2009.

[11] L. Allen, M. W. Beijersbergen, R. C. Spreeuw, and J. P. Woerdman, "Orbital angular momentum of light and the transformation of Laguerre-Gaussian laser modes," *Phys. Rev. A*, vol. 45, pp. 8185–8189, 1992.

[12] A. M. Yao and M. J. Padgett, "Orbital angular momentum: origins, behavior and applications," *Adv. Opt Photon*, vol. 3, pp. 161–204, 2011.

[13] S. Liu, S. Qi, Y. Zhang, et al., "Highly efficient generation of arbitrary vector beams with tunable polarization, phase, and amplitude," *Photon. Res.*, vol. 6, pp. 228–233, 2018.

[14] A. W. Snyder and J. D. Love, *Optical Waveguide Theory*, London, UK, Chapman & Hall, 1983, pp. 248–259.

[15] S. Raghu and F. M. Haldane, "Analogs of quantum-Hall-effect edge states in photonic crystals," *Phys. Rev. A*, vol. 78, p. 033834, 2008.

[16] M. C. Rechtsman, J. M. Zeuner, Y. Plotnik, et al., "Photonic Floquet topological insulators," *Nature*, vol. 496, pp. 196–200, 2013.

[17] L. Lu, J. D. Joannopoulos, and M. Soljačić, "Topological photonics," *Nat. Photonics*, vol. 8, pp. 821–829, 2014.

[18] L. H. Wu and X. Hu, "Scheme for achieving a topological photonic crystal by using dielectric material," *Phys. Rev. Lett.*, vol. 114, p. 223901, 2015.

[19] Y. Yang, Y. F. Xu, T. Xu, et al., "Visualization of a unidirectional electromagnetic waveguide using topological photonic crystals made of dielectric materials," *Phys. Rev. Lett.*, vol. 120, p. 217401, 2018.

[20] T. Ma and G. Shvets, "All-Si valley-Hall photonic topological insulator," *New J. Phys.*, vol. 18, p. 025012, 2016.

[21] J. Noh, W. A. Benalcazar, S. Huang, et al., "Topological protection of photonic mid-gap defect modes," *Nat. Photonics*, vol. 12, pp. 408–415, 2018.

[22] A. El Hassan, F. K. Kunst, A. Moritz, G. Andler, E. J. Bergholtz, and M. Bourennane, "Corner states of light in photonic waveguides," *Nat. Photonics*, vol. 13, pp. 697–700, 2019.

[23] K. Xie, W. Zhang, A. D. Boardman, et al., "Fiber guiding at the Dirac frequency beyond photonic bandgaps," *Light Sci. Appl.*, vol. 4, p. e304, 2015.

[24] L. Lu, H. Gao, and Z. Wang, "Topological one-way fiber of second Chern number," *Nat. Commun.*, vol. 9, pp. 1–7, 2018.

[25] L. Pilozzi, D. Leykam, Z. Chen, and C. Conti, "Topological photonic crystal fibers and ring resonators," *Opt. Lett.*, vol. 45, pp. 1415–1418, 2020.

[26] M. Makwana, R. Wiltshaw, S. Guenneau, and R. Craster, "Hybrid topological guiding mechanisms for photonic crystal fibers," *Opt. Express*, vol. 28, pp. 30871–30888, 2020.

[27] H. Lin and L. Lu, "Dirac-vortex topological photonic crystal fibre," *Light Sci. Appl.*, vol. 9, pp. 1–7, 2020.

[28] X. Wu, Y. Meng, J. Tian, et al., "Direct observation of valley-polarized topological edge states in designer surface plasmon crystals," *Nat. Commun.*, vol. 8, p. 1304, 2017.

[29] J. Noh, S. Huang, K. P. Chen, and M. C. Rechtsman, "Observation of photonic topological valley Hall edge states," *Phys. Rev. Lett.*, vol. 12, p. 063902, 2018.

[30] M. I. Shalaev, W. Walasik, A. Tsukernik, Y. Xu, and N. M. Litchinitser, "Robust topologically protected transport in photonic crystals at telecommunication wavelengths," *Nat. Nanotechnol.*, vol. 14, pp. 31–34, 2019.

[31] X. T. He, E. T. Liang, J. J. Yuan, et al., "A silicon-on-insulator slab for topological valley transport," *Nat. Commun.*, vol. 10, p. 872, 2019.

[32] S. Arora, T. Bauer, R. Barczyk, E. Verhagen, and L. Kuipers, "Direct quantification of topological protection in symmetry-protected photonic edge states at telecom wavelengths," *Light Sci. Appl.*, vol. 10, p. 9, 2021.

[33] Z. Zhang, F. Li, J. Lu, et al., "Broadband photonic topological insulator based on triangular-holes array with higher energy filling efficiency," *Nanophotonics*, vol. 9, pp. 2839–2846, 2020.

[34] W. M. Deng, X. D. Chen, W. J. Chen, F. L. Zhao, and J. W. Dong, "Vortex index identification and unidirectional propagation in Kagome photonic crystals," *Nanophotonics*, vol. 8, pp. 833–840, 2019.

[35] M. Proctor, P. A. Huidobro, S. A. Maier, R. V. Craster, and M. P. Makwana, "Manipulating topological valley modes in plasmonic metasurfaces," *Nanophotonics*, vol. 9, pp. 657–665, 2020.

[36] P. Russell, "Photonic crystal fibers," *Science*, vol. 299, pp. 358–362, 2003.

[37] J. Lu, C. Qiu, L. Ye, et al., "Observation of topological valley transport of sound in sonic crystals," *Nat. Phys.*, vol. 13, pp. 369–374, 2017.

[38] Z. Zhang, J. Gan, X. Heng, et al., "Optical fiber design with orbital angular momentum light purity higher than 99.9%," *Opt. Express*, vol. 23, pp. 29331–29341, 2015.

Supplementary Material: The online version of this article offers supplementary material (https://doi.org/10.1515/nanoph-2021-0395).